Disproportionately large impacts of wildland-urban interface fire emissions on global air quality and human health

Tang, Wenfu; Emmons, Louisa K.; Wiedinmyer, Christine; Partha, Debatosh B.; Huang, Yaoxian; He, Cenlin; Zhang, Junzhe; Barsanti, Kelley C.; Levelt, Pieternel F.; More Authors

DOI
10.1126/sciadv.adr2616

Publication date
2025

Document Version
Final published version

Published in
Science Advances

ATMOSPHERIC SCIENCE

Disproportionately large impacts of wildland-urban interface fire emissions on global air quality and human health

Wenfu Tang[1]*, Louisa K. Emmons[1], Christine Wiedinmyer[2], Debatosh B. Partha[3]†, Yaoxian Huang[3], Cenlin He[4], Junzhe Zhang[5], Kelley C. Barsanti[1,6], Benjamin Gaubert[1], Duseong S. Jo[7], Jun Zhang[1], Rebecca Buchholz[1], Simone Tilmes[1], Francis Vitt[1], Claire Granier[2,8,9], Helen M. Worden[1], Pieternel F. Levelt[1,10,11]

Fires in the wildland-urban interface (WUI) are a global issue with growing importance. However, the impact of WUI fires on air quality and health is less understood compared to that of fires in wildland. We analyze WUI fire impacts on air quality and health at the global scale using a multi-scale atmospheric chemistry model—the Multi-Scale Infrastructure for Chemistry and Aerosols model (MUSICA). WUI fires have notable impacts on key air pollutants [e.g., carbon monoxide (CO), nitrogen dioxide (NO_2), fine particulate matter ($PM_{2.5}$), and ozone (O_3)]. The health impact of WUI fire emission is disproportionately large compared to wildland fires primarily because WUI fires are closer to human settlement. Globally, the fraction of WUI fire–caused annual premature deaths (APDs) to all fire–caused APDs is about three times of the fraction of WUI fire emissions to all fire emissions. The developed model framework can be applied to address critical needs in understanding and mitigating WUI fires and their impacts.

INTRODUCTION

The wildland-urban interface (WUI) is the geographic area where wildland vegetation and land developed by human activity come into contact or intermingle (*1*). Recent studies have found that WUI areas have been expanding in all populated continents, reaching ~5% of global land area in 2020 excluding Antarctica, and are likely to continue increasing in the future (*2*–*4*). The fractions of fire counts and burned area within WUI have increased globally by 23% and 35%, respectively, from 2005 to 2020 mainly due to the WUI area expansion (*3*). Recent examples of global destructive WUI fires include the 2017 Knysna fires in South Africa (*5*), the 2018 Camp Fire in California, USA (*6*), the 2019/2020 Black Summer Fires in Australia (*7*), the 2021 Marshall Fire in Colorado, USA (*8*), the 2022 North Gyeongbuk Province fire in South Korea (*9*), and the 2023 Maui Fire in Hawaii, USA.

Fires in WUI differ from fires outside of WUI (hereafter wildland fires) in several aspects. Fires in WUI areas are by definition overlapping with human development and activities, and therefore are likely to have different ignition patterns, behavior, management strategies, and socioeconomic and health impacts compared to wildland fires (*10*, *11*). In addition, because WUI fires are more likely to involve the burning of structures, vehicles, and their contents (*12*–*15*), fuels burned and thus emissions from WUI fires are also different from wildland fires.

Progress has been made in understanding WUI fire risk [e.g., (*16*–*18*)], WUI fire behavior [e.g., (*8*, *19*)], WUI fire management [e.g., (*20*, *21*)], WUI fire damage [e.g., (*22*)], changes in WUI areas and WUI fires [e.g., (*23*–*25*)], and relevant practices and mitigation and management policies [e.g., (*26*, *27*)]. These advances have been made mostly in limited countries and regions [e.g., (*1*, *19*, *28*–*32*)], leaving the connections between WUI fire risk, behavior, management, and mitigation on climate completely unaddressed in a global context. As for the impacts of WUI fires on air quality and human health, our current state of the knowledge is even more limited, especially compared to wildland fires (*12*–*15*), leaving a substantial knowledge gap at the global scale.

Here, we use the Multi-Scale Infrastructure for Chemistry and Aerosols (MUSICA) model with carbon monoxide (CO) chemical tracers that track emission sources and a recently developed global WUI fire dataset to quantify global impacts of WUI fire emissions on air quality and human health. MUSICA is a state-of-the-art community-coupled climate-chemistry model for simulations of large-scale atmospheric phenomena in a global modeling framework while still resolving chemistry at emission- and exposure-relevant scales (*33*, *34*). Here, we analyze the global impacts of WUI fires on air quality and human exposure over a 1-year period and compare them to impacts of wildland fires, with some additional foci on air pollutants and burn characteristics for the continental United States (CONUS). We show the spatial and temporal features of global WUI fires, followed by other characteristics of WUI fires such as ignition and burning characteristics and chemical characteristics of WUI fire–emitted pollutants. Last, we show the air quality and health impact of WUI fires relative to wildland fires. Note that in this study WUI fires refers to fires located in the WUI area regardless of the involvement of structure or vehicle burning. We

[1]Atmospheric Chemistry Observations and Modeling Laboratory, NSF National Center for Atmospheric Research, Boulder, CO 80301, USA. [2]Cooperative Institute for Research in Environmental Sciences, University of Colorado, Boulder, Boulder, CO 80309, USA. [3]Department of Civil and Environmental Engineering, Wayne State University, Detroit, MI 48202, USA. [4]Research Applications Laboratory, NSF National Center for Atmospheric Research, Boulder, CO 80301, USA. [5]Department of Geography, University of California, Los Angeles, Los Angeles, CA 90095, USA. [6]Department of Chemical and Environmental Engineering, Center for Environmental Research and Technology, University of California, Riverside, Riverside, CA 92521, USA. [7]Department of Earth Science Education, Seoul National University, Seoul, Korea. [8]Laboratoire d'Aérologie, CNRS, Université de Toulouse, Toulouse, France. [9]NOAA Chemical Sciences Laboratory, Boulder, CO 80305, USA. [10]Royal Netherlands Meteorological Institute (KNMI), Utrechtseweg 297, 3730 AE De Bilt, Netherlands. [11]University of Technology Delft, Mekelweg 5, 2628 CD Delft, Netherlands.
*Corresponding author. Email: wenfut@ucar.edu
†Present address: Department of Earth, Environmental and Planetary Science, Northwestern University, Evanston, IL, USA.

conduct a control simulation for the year 2020 that includes both WUI and wildland fires (hereinafter S1–All fires) with respective CO tracers for wildland and WUI fire emissions. We also conduct three additional sensitivity simulations with only WUI fires (hereinafter S2–WUI-fires-only), only wildland fires (hereinafter S3–Wildland-fires-only), and without fires (hereinafter S4–No-fires). The difference between S1–All-fires and S4–No-fires quantifies total fire impacts. The difference between S1–All-fires and S2–WUI-fires-only reveals wildland fire impacts, while the difference between S1–All-fires and S3–Wildland-fires-only indicates WUI fire impacts.

RESULTS

Unique spatial and temporal features of global WUI fire emissions and tracers

While there are some expected similarities in the spatial distribution of WUI fire and wildland fire emissions associated with the occurrence and spread of fires (climate, weather, and fuel conditions), there are some unique features that emerge from our analysis. The difference in spatial distributions of WUI and wildland fire emissions is mainly driven by the distribution of WUI areas and human activities. For example, in the Amazon, the wildland fire emissions are relatively high due to deforestation activities (*35*), while the WUI fire emissions are negligible due to the limited WUI area in the region. In contrast, over Europe, the WUI fire emissions are relatively high due to the large WUI area (Fig. 1C), while wildland fire emissions are much lower compared to global hotspot regions. Over the CONUS, both WUI and wildland fire emissions over the west coast are high. Emissions over some WUI and wildland fire hotspots in California and Oregon are co-located due to large fires that cover both WUI and wildland regions. Over the southeast, WUI fire emissions are as high as those in the west coast due to large WUI area coverage (Fig. 1F), while wildland fire emissions are much smaller than those in the west coast due to less frequent and smaller fires.

In most regions, WUI and wildfire emissions exhibit seasonal signals with similar timing but differing amplitudes (Fig. 2). Over Asia, the WUI and wildland fire signals have a peak in April, while the wildland fire signal has an additional peak in September that is driven by wildland fires in Siberia (fig. S5). Over North America, the WUI fire signal shows a larger peak in April and a smaller peak in November, while the wildland fire signal has a larger peak in September and a smaller peak in May [consistent with a previous study, (*36*)]. The November peak of the WUI fire signal is consistent with (*22*), which indicates that fires with different ignitions (human-related versus lightning) in the western United States have different seasonality. The seasonality over the CONUS also shows large subregional variations (fig. S6). Over the western United States, both WUI and wildland fire signals are higher in September than in other months. Over the central and eastern United States, the peaks around March to April and November are comparable for WUI and wildland fire signals. Over the United States, some of the WUI fires could be prescribed fires that might contribute to the different seasonality between WUI and wildland fires since many prescribed fires happen in the fall, winter, and spring months, depending on the region.

Ignition and burning characteristics of WUI fire

Here, we showed that WUI fires and wildland fires have different ignition types and structure destruction/damage conditions over the CONUS by comparing the modeled fire tracers with the ICS-209-PLUS data product (*37*). Consistent with previous studies looking at ignition characteristics of WUI fires, here we found that the WUI fire signal to wildland fire signal ratio is relatively high for human-ignited

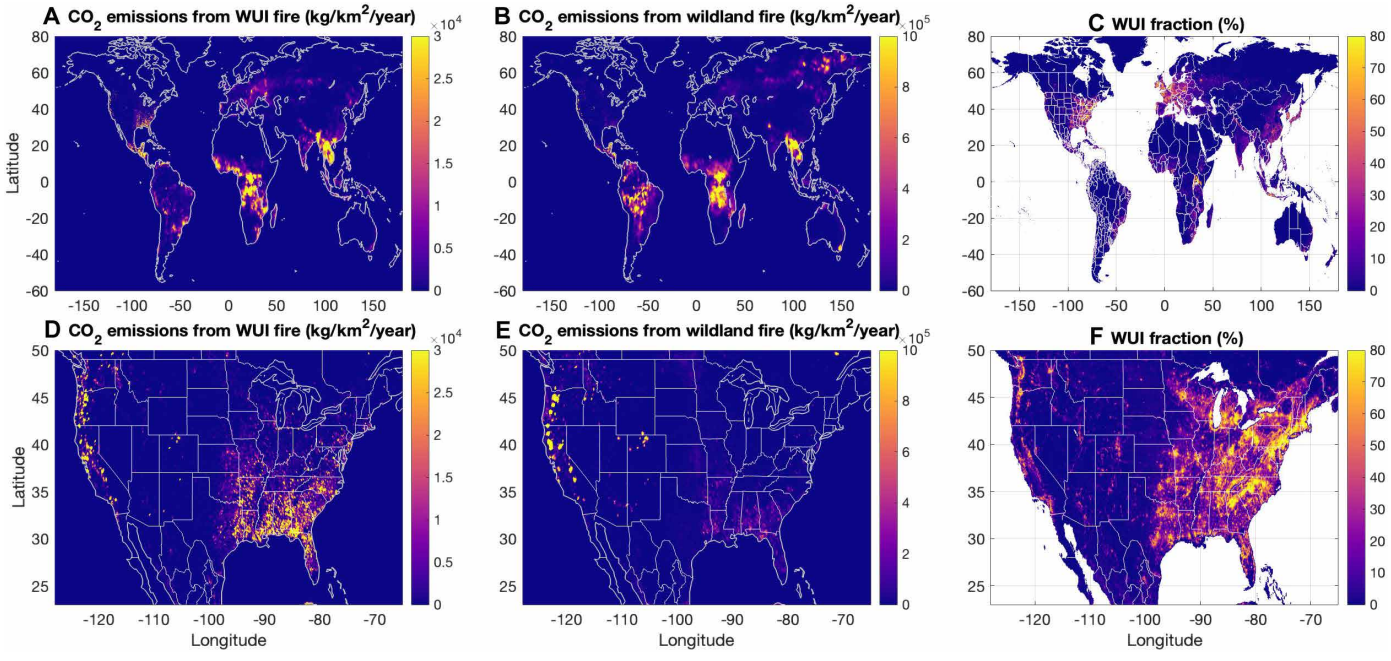

Fig. 1. Spatial distribution of WUI fire and wildland fire emissions. Global annual carbon dioxide (CO_2) emissions from (**A**) wildland-urban interface (WUI) fires and (**B**) wildland fires and (**C**) WUI area fraction from the Worldwide Unified Wildland-Urban Interface (WUWUI) dataset for 2020. Fire emissions are from the Fire INventory from NCAR version 2.5 (FINNv2.5) (*53*). Emissions from FINNv2.5 are separated to WUI and wildland fires by location (see Materials and Methods). (**D** to **F**) Same as (A) to (C) but zoomed in over the continental United States. Note that WUI and wildland fire emission maps have different color scales.

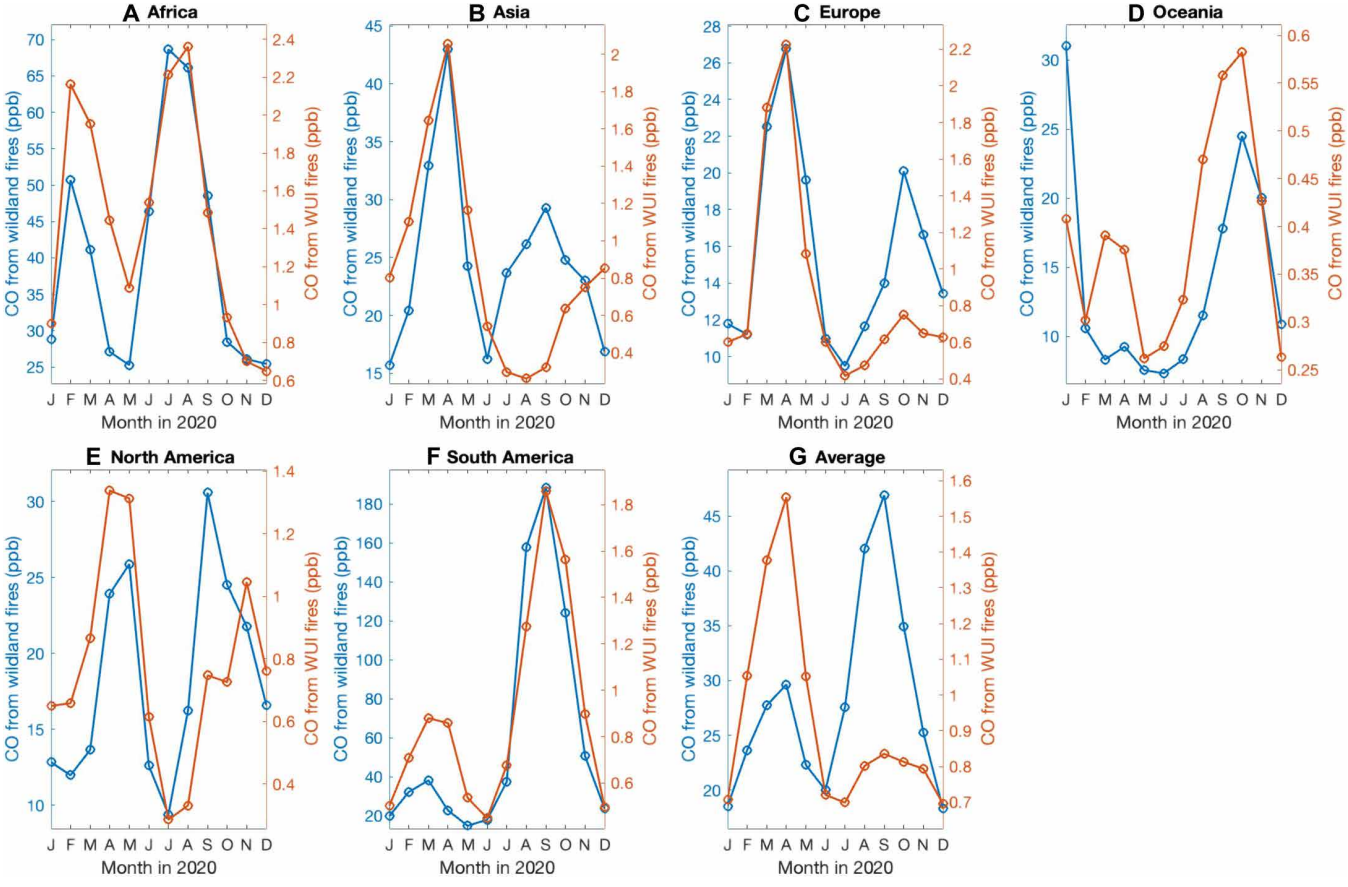

Fig. 2. Seasonality of wildland and WUI fires. Continent-averaged seasonality of wildland fires (blue lines) and WUI fires (red lines) in 2020 over (**A**) Africa, (**B**) Asia, (**C**) Europe, (**D**) Oceania, (**E**) North America, (**F**) South America, and (**G**) average of the six continents. Shown in the figure are the carbon monoxide (CO) tracers of wildland fires and WUI fires (ppb) at the surface from the Multi-Scale Infrastructure for Chemistry and Aerosols model version 0 (MUSICAv0) simulation S1–All-fires.

fires compared to lightning-ignited fires. MUSICAv0 results show that for the human-ignited fires, WUI fire signal mean is 0.08 and the median is 0.05, whereas for lightning-ignited fires, the ratio of WUI fire signal mean is 0.04 and the median is 0.03, indicating that WUI fires are more often caused by human ignition than wildland fires in the CONUS. This is consistent with the previous study (*22*) that concluded that human-ignited wildfires tend to occur close to structures. For structure destruction/damage conditions, the mean WUI fire signal is 0.12 for fires with structure destruction/damage and 0.06 for fires without structure destruction/damage. The mean value for fires with structure destruction/damage is outside the 25% to 75% quantile range of the WUI fire signal to wildland fire signal ratio, indicating that the mean value is dominated by some extremely large WUI fire signal values. For the median, however, the WUI fire signal for fires with and without structure destruction/damage is close (0.045 versus 0.04). Overall, the ignition type is a more obvious characteristic of WUI fire emissions in the CONUS compared to the involvement of structure destruction/damage (Fig. 3). The reason is that although structure burning is a major concern for WUI fires, WUI fires do not always involve structure burning. It is possible that in a WUI fire only the vegetation burns. Determining whether structure burning is involved and the amount of structure fuel that is burned is a great challenge in quantifying WUI fire emissions at large scale (*15*). In addition, emission factors of structure burning may vary substantially due to building style and materials. Even so, this needs to be addressed in future studies to understand emissions of toxics from WUI fires and their health impacts.

Here, we only compared ignition and structure burning involvement for the CONUS due to the availability of ignition and burning data. However, WUI fires in different countries and continents may mean different things. In North America, structure burning and property loss are one of the major concerns for WUI fires. However, in Africa, WUI fires might involve open burning of domestic waste (*38*). We do not have such information at the global scale, and it remains a research question to be addressed to further understand WUI fires and their impacts.

Chemical characteristics of WUI fire–emitted pollutants

The model performance of simulating surface fine particulate matter ($PM_{2.5}$) and ozone (O_3) evaluated against U.S. Environmental Protection Agency (EPA) Air Quality System (AQS) data (Fig. 4) is notably affected when the emissions from WUI fires become more dominant relative to wildland fires. For $PM_{2.5}$, the model performance overall degrades when the ratio of WUI fire signal to wildland fire signal increases, as indicated by the increasing absolute mean bias and decreasing correlation. For O_3, the trend is not as clear as that of $PM_{2.5}$ likely due to the complex O_3 chemistry. However, in the regime with the WUI fire signal less than 0.75, which represents

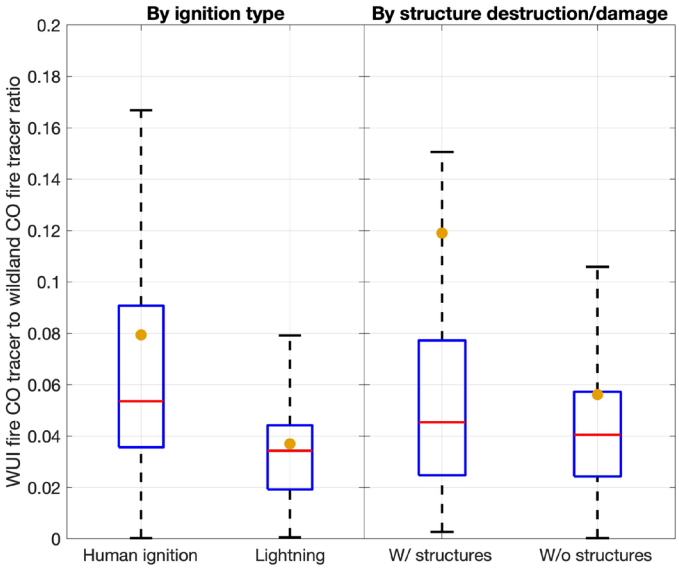

Fig. 3. Differences in ignition type and structure destruction/damage between WUI and wildland fires. Boxplot (with medians represented by red bars, interquartile ranges between 25th and 75th percentiles represented by blue boxes, mean represented by orange dots, and the most extreme data points not considered outliers represented by whiskers) of the ratio of WUI/wildland fire under different ignition types and different structure destruction/damage conditions. Fires from the ICS-209-PLUS data product (*37*) in 2020 are included. The ratio of WUI/wildland fire is represented by the ratio of WUI fire signal to wildland fire signal from the MUSICAv0 simulation S1–All-fires. Surface values of CO tracer from the MUSICAv0 simulation are interpolated to the location and date of fires for analyses.

most of the observed conditions, the model O_3 absolute mean bias increases and correlation decreases with the increasing ratio.

The comparison of model results with measurements as a function of WUI fire influence highlights the importance of and need for further measurement and modeling studies of WUI fires. The degradation of model performance over the CONUS when WUI fires' influence becomes larger can be due to several reasons. First, the locations of WUI fire affected sites can have an impact on model performance. For example, WUI fires are closer to WUI and urban regions where the environment is more complex and challenging for the model to capture (fig. S7). These factors are independent of WUI fires, including the model challenges in capturing complex anthropogenic emissions in such environments and their local transport. Second, it could also be due to the uncertainties in WUI fire emissions (see also Materials and Methods). Emissions from WUI fires are not as well quantified as wildland fires due to the uncertainty in the combustion and emissions from structure burning in current emission inventories. Currently, none of the fire emission inventories explicitly account for structure (or vehicle or other urban fuel) burning. In addition, a potential overestimation of biomass fuel loading and consumption in the WUI fires could also contribute to the model bias. The degradation of model performance in this study points to an urgent need to develop a fire emission inventory and update approaches for estimating fuel loading and consumption in the WUI that includes emissions from the burning of structures and fuels other than vegetation. Several studies have measured emissions from very limited structure and vehicle fires over only a few locations [e.g., (*39*–*42*)]. More measurements are needed to better quantify the emission factors and fuel loads of structure burning in WUI fires to improve fire emission inventories.

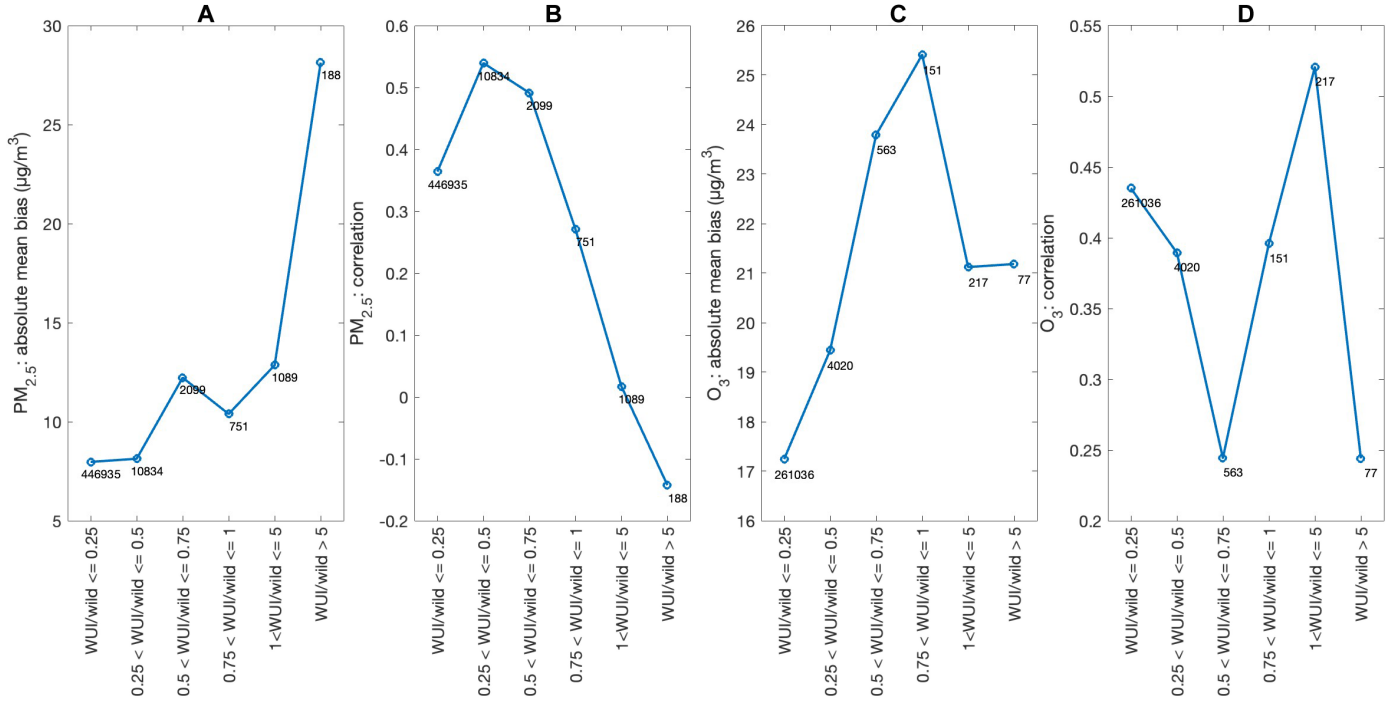

Fig. 4. Model performance under different WUI fire impacts. Model performance (simulation S1–All-fires) evaluated against U.S. Environmental Protection Agency (EPA) Air Quality System (AQS) data under different WUI fire impacts. (**A**) Absolute mean bias of modeled fine particulate matter ($PM_{2.5}$) against EPA AQS $PM_{2.5}$ observations. (**B**) Correlation between modeled $PM_{2.5}$ and EPA AQS $PM_{2.5}$ observations. (**C** and **D**) Same as (A) and (B) but for ozone (O_3). Only sites and days that are significantly affected by fires (i.e., MUSICA simulations S1–All-fires and S4–No-fires are significantly different for the site and the day; *P* value less than 0.1) are included. Numbers labeled in the figure are total data points in the category. WUI/wild is the ratio of WUI fire signal to wildland fire signal.

Impacts of WUI fires on global air quality

WUI fires have notable impacts on annually averaged surface concentrations of key air pollutants such as CO, nitrogen dioxide (NO_2), $PM_{2.5}$, and O_3 (Fig. 5), with uneven spatial distribution globally. The distribution of WUI area (Fig. 1) is not the only driving factor of the distribution of WUI fire impacts, with a spatial correlation of 0.1 to 0.2 between the WUI area fraction and the surface concentrations of these four pollutants. The WUI fires are affected by climate, weather, and fuel conditions, similar to wildland fires, but are more strongly affected by human activities (*11*, *43*, *44*). In addition, since WUI fires by definition are adjacent to urban areas, they will generally affect large and varying populated areas. Over central Africa and Southeast Asia, WUI fire impacts are relatively large, especially for CO and $PM_{2.5}$. The WUI fire impacts on surface NO_2 and $PM_{2.5}$ appears more localized over source regions than CO and O_3 that show global changes. For CO, this is mainly due to its longer lifetime (1 to 2 months), while the long-range transport of O_3 precursors and the change of atmospheric oxidation conditions by WUI fire emissions contribute to the wider spatial impact of O_3 from WUI fires. Over the CONUS, WUI fire impacts mainly concentrate on southeast United States, where the WUI area is large, and the west coast of United States, where large fires are more frequent. Moreover, during certain short periods, WUI fire impacts can be an order of magnitude larger than the aforementioned annual mean values (figs. S1 to S4).

Disproportionately large health impacts of WUI fires

The fractional contributions of WUI fire emissions to all fire emissions are 3.4% for Africa, 3.4% for Asia, 11.4% for Europe, 3.3% for Oceania, 6.0% for North America, 1.3% for South America, and 3.1% for the average of the six populated continents (Fig. 6). However, the fractional contributions of WUI fire emissions to annual premature deaths (APDs) are 5.5% for Africa, 9.4% for Asia, 13.7% for Europe, 8.9% for Oceania, 9.3% for North America, 5.0% for South America, and 8.8% for the average of the six populated continents (Fig. 6A). At the global scale, the fraction of WUI fire emission–induced APD is about three times of the fraction of WUI fire emissions. This disproportionately large health impact of WUI fires relative to emissions is because WUI fires are closer to human settlement. Emissions from WUI fires can have a larger impact on $PM_{2.5}$ and O_3 over the populated regions compared to equal wildland fire emission amounts located far away from the populated region. More details can be found in figs. S8 to S10.

WUI fires tend to have a larger contribution to APD in WUI and urban areas compared to other regions. Since urban and WUI areas are projected to continue to increase in the future, this further motivates to advance the understanding and quantification of WUI fires and impacts. Here, we only quantified health impacts of WUI fires related to O_3 and $PM_{2.5}$. The health impact of WUI fires is expected to be even more important as we expect that structure burning can emit more toxic air pollutants (*15*).

DISCUSSION

Fires in WUI are becoming increasingly important globally. However, their impact on air quality and health is not well understood at continental and global scales. Here, we used the MUSICA model (MUSICAv0) and a recently developed global WUI fire dataset to quantify the global impact of WUI fires versus wildland fires in 2020. This study is subject to uncertainties (see Materials and Methods). A global emission inventory for structure burning is in urgent need, albeit very challenging to better refine the air quality and health impacts of WUI fires. More regional studies with higher model resolution should also follow to further quantify regional impacts. More follow-up studies are also needed to understand the future change of WUI fires and their impacts. Nevertheless, this study provides a global assessment of WUI fire impacts on air quality and human health, an area that has been previously unexamined.

Overall, the spatial distributions of WUI fire and wildland fire emissions are similar as they are driven by the same climate, weather, and fuel conditions that favor fire occurrence and spread. Differences in their spatial distributions are due to influences of human activities and WUI area distribution. In most regions, WUI fire and wildland fire emissions exhibit seasonal signals with similar timing but differing amplitudes. Over the United States, some of the WUI

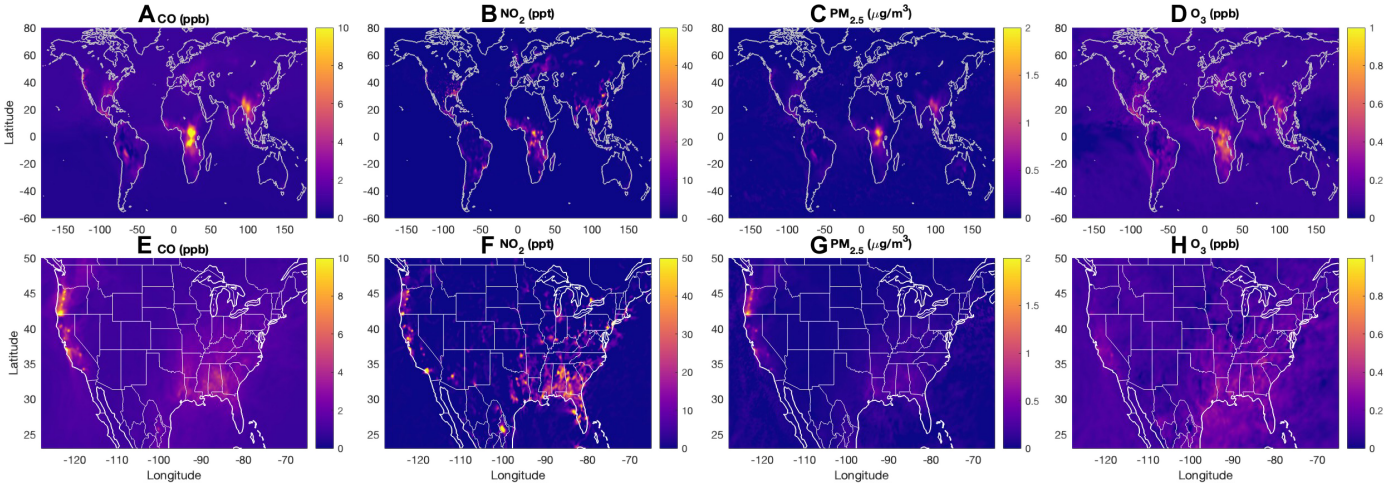

Fig. 5. WUI fire impacts on key pollutants at the surface. Annual average of global (**A**) CO, (**B**) nitrogen dioxide (NO_2), (**C**) $PM_{2.5}$, and (**D**) O_3 at the surface due to WUI fires in 2020. The amounts due to WUI fires are from the difference of S1–All-fires minus S3–Wildland-fires-only. (**E** to **H**) Same as (A) to (D) but zoomed in to the conterminous United States.

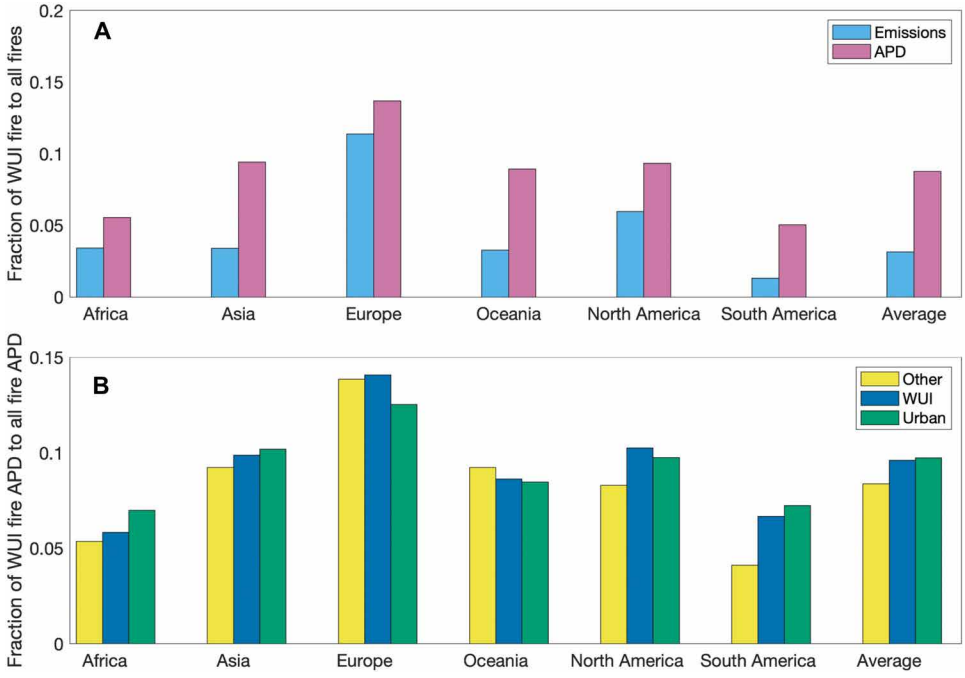

Fig. 6. Disproportionately large impacts of WUI fire emissions on human health. (**A**) Fraction of WUI fire carbon dioxide (CO_2) emissions to all fire CO_2 emissions (blue) and fraction of annual premature deaths (APDs) due to WUI fires to APD due to all fires (pink). (**B**) Fraction of APD due to WUI fires to APD due to all wildfires over WUI (blue), urban (green), and other land type (yellow). Fire CO_2 emissions are from FINNv2.5. WUI data used for calculation are from the WUWUI dataset (*45*). Urban data used for calculation are from the MODIS Land Cover Type Yearly data (MCD12Q1 v6.1). Here, APD includes $PM_{2.5}$ APD due to LRIs and four NCDs (COPD, IHD, stroke, and lung cancer), and O_3 APDs due to COPD.

fires could be prescribed fires that might contribute to the different seasonality. It is important to understand the air quality and health impacts of prescribed burning as it is a commonly used approach to manage fire risk including that in the WUI. Globally, WUI fire emissions have a large peak in April and a smaller peak in September, whereas wildland fire emissions have a large peak in September and a small peak in April. Over the CONUS, WUI and wildland fires are characterized by different ignition types and different fuel types, as some fires in the WUI include nonvegetative fuels (e.g., structures). Differences in fuel types are not considered in this analysis. Model performance in simulating surface air quality degrades when the WUI fire impact becomes dominant over the wildland fire impact, pointing to the necessity of improving fire emission inventories by accounting for structural burning and adjustment of fuel wildland loading and consumption in WUI fires, which is particularly important for estimating impacts of toxics. This is beyond the scope of this study and will be addressed in future studies.

Although WUI fire emissions are small relative to total fire emissions, the health impacts of WUI fire emissions are disproportionately large due to the proximity to human settlement. Here, we looked at $PM_{2.5}$- and O_3-related health impacts. At the global scale, the fraction of WUI fire–induced APDs to all fire–induced APD is about three times the fraction of WUI fire emissions to all fire emissions. Over WUI and urban regions, WUI fires tend to have a larger contribution to APD compared to other areas.

This study provides a global assessment of the impacts of WUI and wildland fires on air quality and human health for 2020. In the future, both the WUI area and the fire activities occurring within WUI are dynamically changing. WUI fires will likely become more important in the future and may have even a larger impact on air quality and health (*45*).

MATERIALS AND METHODS

MUSICAv0 simulations

MUSICAv0 is a variable resolution global model. It is a configuration of the Community Atmospheric Model with chemistry (CAM-chem) (*46*, *47*) that uses a hydrostatic spectral element (SE) dynamical core with an unstructured grid mesh that allows regional refinements (RRs) down to a few kilometers (*48*, *49*). The MUSICAv0 model source code, output files, tutorials, and more information are available at https://www2.acom.ucar.edu/sections/musica-v0.

In our MUSICAv0 simulations, we use the default MOZART-TS1 chemical mechanism, which includes comprehensive tropospheric and stratospheric chemistry with 220 chemical species and 528 reactions (*47*). The aerosol scheme used in MUSICAv0 is the four-mode version of the Modal Aerosol Module [MAM4; (*50*)]. Here, we use a standard configuration of MUSICAv0 that refines to the resolution of ~14 km × 14 km over the conterminous United States, while the resolution outside the refined region is ~111 km × 111 km (i.e., ~1° latitude × 1° longitude) (Fig. 7). Vertically, the configuration has 32 layers.

The simulations in this study are nudged to the Goddard Earth Observing System (GEOS) Model meteorological fields. Specifically, only wind and temperature are nudged with a relaxation time of 6 hours, while dynamic, physical, and radiation processes are calculated by CAM (humidity, clouds, precipitation, convection, etc.). We use the Copernicus Atmosphere Monitoring Service Global Anthropogenic

emissions (CAMS-GLOB-ANTH) version 5.1 (*51*) for anthropogenic emissions and biogenic emissions are calculated online with the Model of Emissions of Gases and Aerosols from Nature version 2.1 [MEGANv2.1; (*47*, *52*)]. For fire emissions, we use the Fire INventory from NCAR version 2.5 [FINNv2.5; (*53*)]. Plume rise climatology is applied following (*54*). FINNv2.5 is described below.

Here, we conduct four MUSICAv0 simulations, namely, S1–All-fires, S2–WUI-fires-only, S3–Wildland-fires-only, and S4–No-fires. In the S1–All-fires simulation, we include CO tracers for WUI fire and wildland fire separately for source attribution. A detailed description of CO tracers can be found in (*55*).

Fire emissions

FINNv2.5 is used as input to the MUSICAv0 simulations. The Fire Inventory from NCAR (FINN) provides daily global estimates of pollutant emissions from open fires with a high spatial and temporal resolution for use in air quality, atmospheric composition, and climate modeling applications (*53*). FINNv2.5 uses active fire detections from both the Moderate Resolution Imaging Spectroradiometer (MODIS) at 1-km resolution and the Visible Infrared Imaging Radiometer Suite (VIIRS) at 375-m spatial resolution for the calculation of fire emissions. FINN calculates daily emissions separately for individual fires and thus makes it possible to separate emissions from WUI and wildland fires.

Fire emissions from FINNv2.5 are separated to WUI fires and wildland fires based on the locations of the individual fires. To do so, we use a global WUI map for 2020 (*56*), which provides global WUI map at 10 m. However, since the resolution of FINN is 375 m and 1 km, we regrid the global WUI map to 1 km. The original data are categorical data (WUI and non-WUI). By regridding the WUI map to a coarser resolution, we calculate the WUI fraction for each 1 km × 1 km grid from the categorical data. For each fire from FINNv2.5, there is an associated WUI fraction. The emissions of WUI fires are calculated by the WUI fraction of the grid that the fire is located in. For example, if the WUI fraction of a grid is 0, then the emissions of the fire are considered wildland fire emissions; if the WUI fraction of a grid is 20%, then 20% of the fire emissions are considered WUI fire emissions, while 80% of the fire emissions are considered wildland fire emissions. This method could introduce uncertainties. However, based on our previous study, this uncertainty is relatively small (*3*).

Note that WUI fires and wildland fires might have different emissions due to the involvement of structure burning. However, emission factors are not the only difference of WUI fires and wildland fires. WUI fires are in general closer to urban area and people, and transport can take less time than wildland fires to reach and influence air quality and exposure. Therefore, although the fraction of WUI fires to wildland fires is relatively small, the WUI fire impacts on air quality and health may be large or even substantial. Although structure burning is a major concern for WUI fires, WUI fires do not always involve structure burning. The information on whether structure burning is involved in WUI fires and the emission factors of structural burning is currently lacking. Here, we mainly focus on different impacts caused by spatiotemporal distribution of WUI fires and subsequent transport of air pollutants, and do not account for differences in emission factors between structural burning and wildland vegetation burning. Previous studies (*13*, *15*) suggested that species like CO_2, CO, and PM (including $PM_{2.5}$ and inhalable PM—PM_{10}) that are produced from all combustion systems are emitted at similar levels from all fuel categories. Therefore, it is reasonable to use the method here. However, emissions of Volatile Organic Compounds (VOCs) and toxics (e.g., polycyclic aromatic hydrocarbons and furans) can be different in magnitude when structure burning is involved. These species are not considered in this study.

Model evaluation

The MUSICAv0 configuration used in this study has been extensively evaluated and validated previously with observations (*34*, *49*, *54*, *57*, *58*). Here, we further evaluate the model with satellite products including the aerosol optical depth (AOD) from MODIS (fig. S11) and CO column retrieval from the Measurements of Pollution in the Troposphere (MOPITT) (fig. S12). The model is also evaluated with TCCON ground-based column CO remote sensing data globally (fig. S13). Specifically over the CONUS, MUSICAv0 surface $PM_{2.5}$ and O_3 are evaluated with the U.S. EPA AQS ground sites (figs. S14 to S15). Although we conducted four MUSICAv0 simulations, here we only evaluate S1–All fires because only S1–All fires is the real-world scenario and can be comparable to observations. Overall, the comparisons show that the model agrees reasonably with observations (see Supplementary Text for detailed descriptions of the evaluation results).

Health impact and exposure calculation

We calculate the annual total premature deaths (APDs) attributable to $PM_{2.5}$ and O_3 exposure following the methodologies used in the recent health studies (*59*, *60*).

For $PM_{2.5}$, we calculate APDs due to lower respiratory infections (LRIs) and four noncommunicable diseases (NCDs), namely, chronic obstructive pulmonary disease (COPD), ischemic heart disease (IHD), stroke, and lung cancer. To quantify the $PM_{2.5}$-induced APDs, we use the Global Exposure Mortality Model (GEMM) developed by

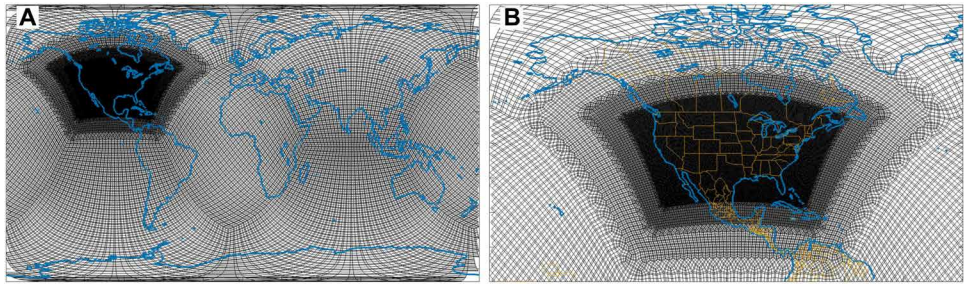

Fig. 7. Model grid used in this study. Model grid of the MUSICAv0 with regional refinement over the conterminous United States. (**A**) Global map. (**B**) Zoomed in over North America.

(*61*), which estimates the hazard ratio (HR) for nonaccidental deaths due to NCDs and LRIs attributable to long-term ambient $PM_{2.5}$ exposure from different sources. In the GEMM model, HR in each longitude (i) and latitude (j) for specific health outcomes (h) and 5-year age interval age groups (a) starting from 25 to 80-year plus ($HR_{i,j,h,a}$) is calculated as a function of annual mean ambient surface $PM_{2.5}$ concentrations ($C_{i,j}$), as shown in Eq. 1.

$$HR_{i,j,h,a} = \exp\left\{\frac{\theta \ln\left(\frac{z_{i,j}}{\alpha}+1\right)}{1+\exp\left(-\frac{z_{i,j}-\mu}{\nu}\right)}\right\}, z_{i,j} = \max\left(0,\ C_{i,j}-C_0\right) \quad (1)$$

where $C_{i,j}$ is the model-simulated annual mean surface $PM_{2.5}$ concentrations, which are retrieved from four different cases of MUSICAv0 model simulations; C_0 is a counterfactual $PM_{2.5}$ concentration as 2.4 $\mu g / m^3$, under which there is no risk of premature deaths due to NCDs associated with long-term $PM_{2.5}$ exposure; θ, α, μ, and ν are GEMM model fit parameters, which are retrieved from 41 global cohorts in 16 different studies incorporated in (*61*). We used the standard errors (SEs) of the GEMM model fit parameter θ to estimate the uncertainty and 95% confidence interval (CI) of APDs attributable to $PM_{2.5}$ exposure.

For O_3, we quantify the APDs attributable to COPD. We calculate the HR associated with O_3-induced COPD (*62*). As shown in Eq. 2, HR in each latitude and longitude grid box ($HR_{i,j}$) is calculated as

$$HR_{i,j} = \exp^{\left(\eta \Delta Y_{i,j}\right)}, \Delta Y_{i,j} = \max\left(0,\quad Y_{i,j}-26.7\right) \quad (2)$$

where η is the log-linear between O_3 concentrations and HR associated with O_3-induced COPD; $Y_{i,j}$ is the annual mean daily maximum 8-hour (MDA8h) O_3 concentration. Turner *et al.* (*62*) reported that the HR associated with COPD increases by 14% (95% CI, 8 to 21%) per 10 parts per billion by volume (ppbv) increase in MDA8h O_3 concentration, which indicates an odds ratio (OR) of 1.14 (95% CI, 1.08 to 1.21), resulting in a mean value of η as 0.0131 (95% CI, 0.0077 to 0.0191). We incorporate the upper and lower η values to estimate the 95% CI of APDs attributable to O_3 exposure. Additionally, we consider a threshold value for MDA8h O_3 concentration as 26.7 ppbv, under which we assume that there will be no premature mortality due to O_3-induced COPD.

The global APD estimates are calculated as a function of the gridded population count (POP), the baseline mortality rate (BMR), and the HR for each health outcome associated with different levels of $PM_{2.5}$ and O_3 exposure. The mathematical equation for quantifying APDs ($APD_{i,j,h,a}$) attributable to $PM_{2.5}$ and O_3 exposure in each grid box (i, j), health outcomes (h), and age group (a) is derived as

$$APD_{i,j,h,a} = POP_{i,j,h,a} \times BMR_{i,j,h,a} \times \left[1-\frac{1}{HR_{i,j,h,a}}\right] \quad (3)$$

where $POP_{i,j,h,a}$ is the global gridded age-and-health-outcome–specific population, which is derived as the product of the total population count in each latitude and longitude and the age-and-health-outcome–specific population fraction. We use the population data for 2020 from the Gridded Population of the World version 4.11 (GPWv4.11; *63*) at the horizontal grid resolution of 2.5 min × 2.5 min, which is regridded to 0.1° latitude by 0.1° longitude. $BMR_{i,j,h,a}$ is the 2020 BMR for each model grid cell (i, j), health endpoint (h), and 5-year age interval (a), which is from the latest 2021 Global Burden of Disease dataset (*64*). For computational efficiency, we follow our previous methods (*59*, *60*, *65*) to divide the globe into 11 regions. We calculate the mean BMR from the Global Burden of Disease (GBD) 2021 datasets for each health endpoint and each 5-year age interval. Within each defined region, we assume the same BMR for each health endpoint and each 5-year age interval in each grid cell. All data, including model-simulated $PM_{2.5}$ and O_3 concentrations, are gridded to 0.1° latitude ×0.1° longitude resolution for the calculation. The global annual total APDs attributable to $PM_{2.5}$ and O_3 exposure are the sum of each global annual total health endpoint and 5-year age intervals. We calculate APDs attributable to $PM_{2.5}$ and O_3 exposure for each set of MUSICAv0 model simulations. For example, the differences between S1–All-fires and S2–WUI-fires-only reveal the net impacts of wildland fires, while the differences between S1–All-fires and S3–Wildland-fires-only lead to the net impacts of WUI fires.

Other data used in this study

EPA AQS

U.S. EPA AQS surface measurements of hourly O_3 and $PM_{2.5}$ for 2020 are used in this study (https://aqs.epa.gov/aqsweb/airdata/download_files.html). The measurements are hourly; however, we only use three-hourly measurements to compare with MUSICAv0 model output. Three-hourly model output from S1–All fires (control) under different fire-impact conditions is interpolated to EPA AQS sites for comparisons. A distribution of EPA AQS sites for O_3 and $PM_{2.5}$ in 2020 can be found in fig. S7.

ICS-209-PLUS data product

ICS-209-PLUS is a dataset mined from the public archive (1999–2020) of the U.S. National Incident Management System Incident Status Summary (ICS-209) forms that include 34,478 wildland fires (*37*). The data are available at https://zenodo.org/records/7036299. A wildfire is generally considered large enough to require an ICS-209 report when it exceeds 100 acres in timber or 300 acres in grass or brush. These fires account for only a small portion of fire counts; however, they account for most of the burned area in the United States. ICS-209-PLUS provides ignition source (lightning versus human ignition) and information on structure burning. We compare these fires events in 2020 from ICS-209-PLUS (1386 fires) to our model results.

Urban distribution data from MODIS

Land Cover Type Yearly data for 2020 from MODIS/Terra+Aqua (MCD12Q1 v6.1) (*66*) are used to show urban distribution. The MCD12Q1 data are available at https://lpdaac.usgs.gov/products/mcd12q1v061/ (accessed 16 November 2023). The original resolution of these data is ~500 m. Urban and buildup is one of the categories of the Land Cover Type dataset. We regrid the data to ~9 km (1/12° latitude × 1/12° longitude) resolution for plotting in this paper. By regridding to a coarser resolution, we calculate urban cover fraction from the category data.

WUWUI dataset

The Worldwide Unified Wildland-Urban Interface (WUWUI) database is a global 9-km dataset for global WUI area fractions. WUWUI is developed using machine learning based on the global WUI map for 2020 at 10-m resolution (*56*). WUWUI agrees well with other global WUI datasets (*4*, *56*) and provides global WUI area fractions for the year 2001, 2005, 2010, 2015, and 2020 (*3*, *45*).

MOPITT CO retrievals

The MOPITT instrument onboard the NASA Terra satellite provides both thermal-infrared (TIR) and near-infrared (NIR) radiance

measurements since March 2000. Retrievals of CO column density and vertical profiles are provided in a multispectral TIR-NIR joint product, which has sensitivity to near-surface as well as free tropospheric CO. Here, we use the MOPITT Version 9 Level 2 CO column product (*67*).

TCCON CO vertical column

TCCON is a network of ground-based Fourier transform spectrometers that records direct solar spectra in the NIR spectral region (*68*, *69*). CO vertical column data (ppb) from 23 TCCON sites are used.

Uncertainty discussion

Our modeling studies are subject to uncertainties.

1) WUI data can be subject to uncertainties, and the WUI definition and map can vary with practice and application (*70*, *71*). Here, we use a state-of-the-art global high-resolution WUI map (*2*) with consistently defined WUI at the global scale.

2) Fire emission inventories are subject to uncertainties. FINNv2.5 overall agrees reasonably well with other global fire inventories (*53*) but tends to have higher emissions over Congo and Amazon. Not considering structure burning emissions is another source of uncertainties. To our knowledge, there is no existing global fire emission inventory that explicitly accounts for structure burning. Although previous studies found that species like CO_2, CO, and PM (including $PM_{2.5}$ and inhalable PM—PM_{10}) that are produced from all combustion systems are emitted at similar levels from all fuel categories, emissions of VOCs and toxics can be substantially different, which can further affect O_3. Quantifying structure burning emissions at global scale is extremely challenging yet important. We hope that the large WUI fire impacts on air quality and health revealed in this study can motivate the development of such an inventory.

3) We combine the FINNv2.5 fire emission inventory and the WUI map at 1-km spatial resolution. The 1-km resolution limitation comes from the spatial resolution of satellite fire detection data. At the county level or in some developed countries, there might be bottom-up information on fires with more details that have much higher resolution than 1 km. However, at global scale, we can only rely on satellite fire products. FINNv2.5 combines VIIRS and MODIS active fire products to calculate fire emissions at the pixel size of 1 km. To our knowledge, FINNv2.5 with 1-km resolution has the highest resolution among global fire emission inventories. In our previous study (*3*), we quantified how the WUI fire fraction changes with spatial resolutions at which the fire data and WUI data are merged. We merged fire data and WUI data at 1 km, 4 km, 9 km, and 1° resolution and found that in 2020 the calculated WUI fire count fractions are 4.3%, 4.3%, 4.3%, and 4.8%, respectively. This indicates that the calculation of WUI fire emissions is not sensitive to the resolution at the kilometer-scale resolution. Therefore, we merge FINNv2.5 fire emission inventory and the WUI map at 1-km resolution, although the model simulation is 14 km and 1° resolution.

4) Model simulations are subject to uncertainties, where the spatial resolution outside CONUS is relatively coarse (~1°). We evaluate the model results with observations (figs. S11 to S15; see also above for discussions) with multiple observation datasets, and the model performance is reasonable. The modeled air pollutants' concentrations and population data are both re-gridded to 0.1° × 0.1° spatial resolution to calculate health impact. While it is common practice to regrid data with different resolutions for calculation, to understand the uncertainties in this process (merging coarse-resolution modeled air pollution data with high-resolution population data), we conduct additional analyses (Supplementary Materials, figs. S16 and S17, and table S1) by calculating population-weighted exposure levels of $PM_{2.5}$ and O_3 with different resolutions (see the Supplementary Materials for more detailed discussions). The results indicate that the uncertainties from using the coarse-resolution modeled air pollution fields with high-resolution population data are relatively small (~10% for WUI fire impacts and ~20% for wildland fire impacts) at large scale (such as the global and continental scale analyzed in this study). However, at the regional scale, higher model spatial resolution is needed to resolve regional features of air pollution distribution. More future studies focusing on regional-to-local scales with high resolution (e.g., kilometer-scale) are needed to refine the results from this study.

Supplementary Materials

This PDF file includes:

Supplementary Text S1 and S2
Figs. S1 to S17
Table S1
References

REFERENCES AND NOTES

1. S. I. Stewart, V. C. Radeloff, R. B. Hammer, T. J. Hawbaker, Defining the wildland–urban interface. *J. For.* **105**, 201–207 (2007).
2. F. Schug, A. Bar-Massada, A. R. Carlson, H. Cox, T. J. Hawbaker, D. Helmers, P. Hostert, D. Kaim, N. K. Kasraee, S. Martinuzzi, M. H. Mockrin, The global wildland–urban interface. *Nature* **621**, 94–99 (2023).
3. W. Tang, C. He, L. Emmons, J. Zhang, Global expansion of wildland-urban interface (WUI) and WUI fires: Insights from a multiyear worldwide unified database (WUWUI). *Environ. Res. Lett.* **19**, 044028 (2024).
4. B. Chen, S. Wu, Y. Jin, Y. Song, C. Wu, S. Venevsky, B. Xu, C. Webster, P. Gong, Wildfire risk for global wildland–urban interface areas. *Nat. Sustain.* **7**, 474–484 (2024).
5. N. F. Quiroz, L. Gibson, W. S. Conradie, P. Ryan, R. Heydenrych, A. Moran, A. van Straten, R. Walls, Analysis of the 2017 Knysna fires disaster with emphasis on fire spread, home losses and the influence of vegetation and weather conditions: A South African case study. *Int. J. Disaster Risk Reduct.* **88**, 103618 (2023).
6. A. Chulahwat, H. Mahmoud, S. Monedero, F. J. Diez Vizcaíno, J. Ramirez, D. Buckley, A. C. Forradellas, Integrated graph measures reveal survival likelihood for buildings in wildfire events. *Sci. Rep.* **12**, 15954 (2022).
7. N. Levin, M. Yebra, S. Phinn, Unveiling the factors responsible for Australia's Black Summer fires of 2019/2020. *Fire* **4**, 58 (2021).
8. T. W. Juliano, N. Lareau, M. E. Frediani, K. Shamsaei, M. Eghdami, K. Kosiba, J. Wurman, A. DeCastro, B. Kosović, H. Ebrahimian, Toward a better understanding of wildfire behavior in the wildland-urban interface: A case study of the 2021 Marshall fire. *Geophys. Res. Lett.* **50**, e2022GL101557 (2023).
9. H. Park, K. Nam, H. Lim, Is critical infrastructure safe from wildfires? A case study of wildland-industrial and-urban interface areas in South Korea. *Int. J. Disaster Risk Reduct.* **95**, 103849 (2023).
10. W. E. Mell, S. L. Manzello, A. Maranghides, D. Butry, R. G. Rehm, The wildland–urban interface fire problem–current approaches and research needs. *Int. J. Wildland Fire.* **19**, 238–251 (2010).
11. M. Calviño-Cancela, M. L. Chas-Amil, E. D. García-Martínez, J. Touza, Wildfire risk associated with different vegetation types within and outside wildland-urban interfaces. *For. Ecol. Manage.* **372**, 1–9 (2016).
12. W. E. Cascio, Wildland fire smoke and human health. *Sci. Total Environ.* **624**, 586–595 (2018).
13. D. A. Jaffe, S. M. O'Neill, N. K. Larkin, A. L. Holder, D. L. Peterson, J. E. Halofsky, A. G. Rappold, Wildfire and prescribed burning impacts on air quality in the United States. *J. Air Waste Manag. Assoc.* **70**, 583–615 (2020).
14. M. E. Harries, D. T. Allen, O. Adetona, M. L. Bell, M. S. Black, J. L. Burgess, F. L. Dryer, A. L. Holder, A. Mascareñas, F. L. Rosario-Ortiz, A. A. Stec, A research agenda for the chemistry of fires at the wildland–urban interface: A National Academies consensus report. *Environ. Sci. Technol.* **56**, 15189–15191 (2022).
15. A. L. Holder, A. Ahmed, J. M. Vukovich, V. Rao, Hazardous air pollutant emissions estimates from wildfires in the wildland urban interface. *PNAS Nexus* **2**, pgad186 (2023).
16. Z. Liu, M. C. Wimberly, A. Lamsal, T. L. Sohl, T. J. Hawbaker, Climate change and wildfire risk in an expanding wildland–urban interface: A case study from the Colorado Front Range Corridor. *Landsc. Ecol.* **30**, 1943–1957 (2015).

17. V. C. Radeloff, D. P. Helmers, H. A. Kramer, M. H. Mockrin, P. M. Alexandre, A. Bar-Massada, V. Butsic, T. J. Hawbaker, S. Martinuzzi, A. D. Syphard, S. I. Stewart, Rapid growth of the US wildland-urban interface raises wildfire risk. *Proc. Natl. Acad. Sci. U.S.A.* **115**, 3314–3319 (2018).
18. H. Mahmoud, A. Chulahwat, Assessing wildland–urban interface fire risk. *R. Soc. Open Sci.* **7**, 201183 (2020).
19. O. Price, R. Bradstock, Countervailing effects of urbanization and vegetation extent on fire frequency on the Wildland Urban Interface: Disentangling fuel and ignition effects. *Landscape Urban Plan.* **130**, 81–88 (2014).
20. R. B. Hammer, S. I. Stewart, V. C. Radeloff, Demographic trends, the wildland–urban interface, and wildfire management. *Soc. Nat. Resour.* **22**, 777–782 (2009).
21. C. I. Roos, T. W. Swetnam, T. J. Ferguson, M. J. Liebmann, R. A. Loehman, J. R. Welch, E. Q. Margolis, C. H. Guiterman, W. C. Hockaday, M. J. Aiuvalasit, J. Battillo, Native American fire management at an ancient wildland–urban interface in the Southwest United States. *Proc. Natl. Acad. Sci. U.S.A.* **118**, e2018733118 (2021).
22. P. E. Higuera, M. C. Cook, J. K. Balch, E. N. Stavros, A. L. Mahood, L. A. St. Denis, Shifting social-ecological fire regimes explain increasing structure loss from Western wildfires. *PNAS Nexus* **2**, pgad005 (2023).
23. D. M. Theobald, W. H. Romme, Expansion of the US wildland–urban interface. *Landscape Urban Plan.* **83**, 340–354 (2007).
24. M. Burke, A. Driscoll, S. Heft-Neal, J. Xue, J. Burney, M. Wara, The changing risk and burden of wildfire in the United States. *Proc. Natl. Acad. Sci. U.S.A.* **118**, e2011048118 (2021).
25. A. Ganteaume, R. Barbero, M. Jappiot, E. Maillé, Understanding future changes to fires in southern Europe and their impacts on the wildland-urban interface. *J. Saf. Sci. Resilience* **2**, 20–29 (2021).
26. S. L. Stephens, M. A. Adams, J. Handmer, F. R. Kearns, B. Leicester, J. Leonard, M. A. Moritz, Urban–wildland fires: How California and other regions of the US can learn from Australia. *Environ. Res. Lett.* **4**, 014010 (2009).
27. E. Ronchi, S. M. Gwynne, G. Rein, P. Intini, R. Wadhwani, An open multi-physics framework for modelling wildland-urban interface fire evacuations. *Saf. Sci.* **118**, 868–880 (2019).
28. L. M. Johnston, M. D. Flannigan, Mapping Canadian wildland fire interface areas. *Int. J. Wildland Fire.* **27**, 1–14 (2017).
29. S. Modugno, H. Balzter, B. Cole, P. Borrelli, Mapping regional patterns of large forest fires in Wildland–Urban Interface areas in Europe. *J. Environ. Manage.* **172**, 112–126 (2016).
30. L. Galiana-Martin, G. Herrero, J. Solana, A wildland–urban interface typology for forest fire risk management in Mediterranean areas. *Landscape Res.* **36**, 151–171 (2011).
31. G. Herrero-Corral, M. Jappiot, C. Bouillon, M. Long-Fournel, Application of a geographical assessment method for the characterization of wildland–urban interfaces in the context of wildfire prevention: A case study in western Madrid. *Appl. Geogr.* **35**, 60–70 (2012).
32. P. Sarricolea, R. Serrano-Notivoli, M. Fuentealba, M. Hernández-Mora, F. De la Barrera, P. Smith, Ó. Meseguer-Ruiz, Recent wildfires in Central Chile: Detecting links between burned areas and population exposure in the wildland urban interface. *Sci. Total Environ.* **706**, 135894 (2020).
33. G. G. Pfister, S. D. Eastham, A. F. Arellano, B. Aumont, K. C. Barsanti, M. C. Barth, A. Conley, N. A. Davis, L. K. Emmons, J. D. Fast, A. M. Fiore, The multi-scale infrastructure for chemistry and aerosols (MUSICA). *Bull. Am. Meteorol. Soc.* **101**, E1743–E1760 (2020).
34. W. Tang, G. G. Pfister, R. Kumar, M. Barth, D. P. Edwards, L. K. Emmons, S. Tilmes, Capturing high-resolution air pollution features using the multi-scale infrastructure for chemistry and aerosols version 0 (MUSICAv0) Global modeling system. *J. Geophys. Res. Atmos.* **128**, e2022JD038345 (2023).
35. W. Tang, A. F. Arellano Jr., Investigating dominant characteristics of fires across the Amazon during 2005–2014 through satellite data synthesis of combustion signatures. *J. Geophys. Res. Atmos.* **122**, 1224–1245 (2017).
36. R. R. Buchholz, M. Park, H. M. Worden, W. Tang, D. P. Edwards, B. Gaubert, M. N. Deeter, T. Sullivan, M. Ru, M. Chin, R. C. Levy, New seasonal pattern of pollution emerges from changing North American wildfires. *Nat. Commun.* **13**, 2043 (2022).
37. L. A. St. Denis, K. C. Short, K. McConnell, M. C. Cook, N. P. Mietkiewicz, M. Buckland, J. K. Balch, All-hazards dataset mined from the US National Incident Management System 1999–2020. *Sci. Data* **10**, 112 (2023).
38. C. Wiedinmyer, R. J. Yokelson, B. K. Gullett, Global emissions of trace gases, particulate matter, and hazardous air pollutants from open burning of domestic waste. *Environ. Sci. Technol.* **48**, 9523–9530 (2014).
39. P. Blomqvist, L. Rosell, M. Simonson, Emissions from fires part II: Simulated room fires. *Fire Technol.* **40**, 59–73 (2004).
40. K. W. Fent, D. E. Evans, K. Babik, C. Striley, S. Bertke, S. Kerber, D. Smith, G. P. Horn, Airborne contaminants during controlled residential fires. *J. Occup. Environ. Hyg.* **15**, 399–412 (2018).
41. R. G. Gann, J. D. Averill, E. L. Johnsson, M. R. Nyden, R. D. Peacock, Fire effluent component yields from room-scale fire tests. *Fire Mater.* **34**, 285–314 (2010).
42. H. Wichmann, W. Lorenz, M. Bahadir, Release of PCDD/F and PAH during vehicle fires in traffic tunnels. *Chemosphere* **31**, 2755–2766 (1995).
43. M. C. Wimberly, Z. Liu, Interactions of climate, fire, and management in future forests of the Pacific Northwest. *For. Ecol. Manage.* **327**, 270–279 (2014).
44. D. M. Fox, P. Carrega, Y. Ren, P. Caillouet, C. Bouillon, S. Robert, How wildfire risk is related to urban planning and Fire Weather Index in SE France (1990–2013). *Sci. Total Environ.* **621**, 120–129 (2018).
45. W. Tang. Worldwide Unified Wildland-Urban Interface (WUWUI) database (version v2), Zenodo (2024b). https://doi.org/10.5281/zenodo.10703310.
46. S. Tilmes, A. Hodzic, L. K. Emmons, M. J. Mills, A. Gettelman, D. E. Kinnison, M. Park, J.-F. Lamarque, F. Vitt, M. Shrivastava, P. Campuzano-Jost, J. L. Jimenez, X. Liu, Climate forcing and trends of organic aerosols in the community earth system model (CESM2). *J. Adv. Model. Earth Syst.* **11**, 4323–4351 (2019).
47. L. K. Emmons, R. H. Schwantes, J. J. Orlando, G. Tyndall, D. Kinnison, J. Lamarque, D. Marsh, M. J. Mills, S. Tilmes, C. Bardeen, R. R. Buchholz, A. Conley, A. Gettelman, R. Garcia, I. Simpson, D. R. Blake, S. Meinardi, G. Pétron, The chemistry mechanism in the community earth system model version 2 (CESM2). *J. Adv. Model. Earth Syst.* **12**, e2019MS001882 (2020).
48. P. H. Lauritzen, R. D. Nair, A. R. Herrington, P. Callaghan, S. Goldhaber, J. M. Dennis, J. T. Bacmeister, B. E. Eaton, C. M. Zarzycki, M. A. Taylor, P. A. Ullrich, T. Dubos, A. Gettelman, R. B. Neale, B. Dobbins, K. A. Reed, C. Hannay, B. Medeiros, J. J. Benedict, J. J. Tribbia, NCAR release of CAM-SE in CESM2.0: A reformulation of the spectral element dynamical core in dry-mass vertical coordinates with comprehensive treatment of condensates and energy. *J. Adv. Model. Earth Syst.* **10**, 1537–1570 (2018).
49. R. H. Schwantes, F. G. Lacey, S. Tilmes, L. K. Emmons, P. H. Lauritzen, S. Walters, P. Callaghan, C. M. Zarzycki, M. C. Barth, D. S. Jo, J. T. Bacmeister, R. B. Neale, F. Vitt, E. Kluzek, B. Roozitalab, S. R. Hall, K. Ullmann, C. Warneke, J. Peischl, I. B. Pollack, F. Flocke, G. M. Wolfe, T. F. Hanisco, F. N. Keutsch, J. Kaiser, T. P. V. Bui, J. L. Jimenez, P. Campuzano-Jost, E. C. Apel, R. S. Hornbrook, A. J. Hills, B. Yuan, A. Wisthaler, Evaluating the impact of chemical complexity and horizontal resolution on tropospheric ozone over the conterminous US with a global variable resolution chemistry model. *J. Adv. Model. Earth Syst.* **14**, e2021MS002889 (2022).
50. X. Liu, P.-L. Ma, H. Wang, S. Tilmes, B. Singh, R. C. Easter, S. J. Ghan, P. J. Rasch, Description and evaluation of a new four-mode version of the Modal Aerosol Module (MAM4) within version 5.3 of the Community Atmosphere Model. *Geosci. Model Dev.* **9**, 505–522 (2016).
51. A. Soulié, C. Granier, S. Darras, N. Zilbermann, T. Doumbia, M. Guevara, J.-P. Jalkanen, S. Keita, C. Liousse, M. Crippa, D. Guizzardi, R. Hoesly, S. Smith, Global anthropogenic emissions (CAMS-GLOB-ANT) for the Copernicus Atmosphere Monitoring Service simulations of air quality forecasts and reanalyses. *Earth Syst. Sci. Data.* **16**, 2261–2279 (2023).
52. A. B. Guenther, X. Jiang, C. L. Heald, T. Sakulyanontvittaya, T. Duhl, L. K. Emmons, X. Wang, The Model of Emissions of Gases and Aerosols from Nature version 2.1 (MEGAN2.1): An extended and updated framework for modeling biogenic emissions. *Geosci. Model Dev.* **5**, 1471–1492 (2012).
53. C. Wiedinmyer, Y. Kimura, E. C. McDonald-Buller, L. K. Emmons, R. R. Buchholz, W. Tang, K. Seto, M. B. Joseph, K. C. Barsanti, A. G. Carlton, R. Yokelson, The Fire Inventory from NCAR version 2.5: An updated global fire emissions model for climate and chemistry applications. *Geosci. Model Dev.* **16**, 3873–3891 (2023).
54. W. Tang, L. K. Emmons, R. R. Buchholz, C. Wiedinmyer, R. H. Schwantes, C. He, R. Kumar, G. G. Pfister, H. M. Worden, R. S. Hornbrook, E. C. Apel, Effects of fire diurnal variation and plume rise on US air quality during FIREX-AQ and WE-CAN based on the Multi-Scale Infrastructure for Chemistry and Aerosols (MUSICAv0). *J. Geophys. Res. Atmos.* **127**, e2022JD036650 (2022).
55. W. Tang, L. K. Emmons, A. F. Arellano Jr., B. Gaubert, C. Knote, S. Tilmes, R. R. Buchholz, G. G. Pfister, G. S. Diskin, D. R. Blake, N. J. Blake, Source contributions to carbon monoxide concentrations during KORUS-AQ based on CAM-chem model applications. *J. Geophys. Res. Atmos.* **124**, 2796–2822 (2019).
56. F. Schug, A. Bar-Massada, A. R. Carlson, H. Cox, T. J. Hawbaker, D. Helmers, P. Hoster, D. Kaim, N. K. Kasraee, S. Martinuzzi, M. H. Mockrin, K. A. Pfoch, V. C. Radeloff. Map of the global wildland-urban interface (1.1), Zenodo (2023). https://doi.org/10.5281/zenodo.7941460.
57. D. S. Jo, L. K. Emmons, P. Callaghan, S. Tilmes, J. H. Woo, Y. Kim, J. Kim, C. Granier, A. Soulié, T. Doumbia, S. Darras, Comparison of urban air quality simulations during the KORUS-AQ campaign with regionally refined versus global uniform grids in the multi-scale infrastructure for chemistry and aerosols (MUSICA) version 0. *J. Adv. Model. Earth Syst.* **15**, e2022MS003458 (2023).
58. W. Tang, L. K. Emmons, H. M. Worden, R. Kumar, C. He, B. Gaubert, Z. Zheng, S. Tilmes, R. R. Buchholz, S.-E. Martinez-Alonso, C. Granier, A. Soulie, K. McKain, B. C. Daube, J. Peischl, C. Thompson, P. Levelt, Application of the Multi-Scale Infrastructure for Chemistry and Aerosols version 0 (MUSICAv0) for air quality research in Africa. *Geosci. Model Dev.* **16**, 6001–6028 (2023).
59. Y. Huang, D. B. Partha, K. Harper, C. Heyes, Impacts of global solid biofuel stove emissions on ambient air quality and human health. *GeoHealth* **5**, e2020GH000362 (2021).

60. Y. Xiong, D. Partha, N. Prime, S. J. Smith, N. Mariscal, H. Salah, Y. Huang, Long-term trends of impacts of global gasoline and diesel emissions on ambient $PM_{2.5}$ and O_3 pollution and the related health burden for 2000–2015. *Environ. Res. Lett.* **17**, 104042 (2022).
61. R. Burnett, H. Chen, M. Szyszkowicz, N. Fann, B. Hubbell, C. A. Pope III, J. S. Apte, M. Brauer, A. Cohen, S. Weichenthal, J. Coggins, Global estimates of mortality associated with long-term exposure to outdoor fine particulate matter. *Proc. Natl. Acad. Sci. U.S.A.* **115**, 9592–9597 (2018).
62. M. C. Turner, M. Jerrett, C. A. Pope III, D. Krewski, S. M. Gapstur, W. R. Diver, B. S. Beckerman, J. D. Marshall, J. Su, D. L. Crouse, R. T. Burnett, Long-term ozone exposure and mortality in a large prospective study. *Am. J. Respir. Crit. Care Med.* **193**, 1134–1142 (2016).
63. Gridded Population of the World, Version 4 (GPWv4): Population density, revision 11. Columbia University (2018). https://doi.org/10.7927/H49C6VHW.
64. GBD 2021 Risk Factors Collaborators. Global burden and strength of evidence for 88 risk factors in 204 countries and 811 subnational locations, 1990–2021: A systematic analysis for the Global Burden of Disease Study 2021. 2024. https://ncdrisc.org/.
65. Y. Huang, N. Unger, K. Harper, C. Heyes, Global climate and human health effects of the gasoline and diesel vehicle fleets. *GeoHealth* **4**, e2019GH000240 (2020).
66. M. Friedl, D. Sulla-Menashe. MCD12Q1 MODIS/Terra+Aqua Land Cover Type Yearly L3 Global 500m SIN Grid V006, NASA EOSDIS Land Processes DAAC (2019). https://doi.org/10.5067/MODIS/MCD12Q1.006.
67. M. Deeter, G. Francis, J. Gille, D. Mao, S. Martínez-Alonso, H. Worden, D. Ziskin, J. Drummond, R. Commane, G. Diskin, K. McKain, The MOPITT Version 9 CO product: Sampling enhancements and validation. *Atmos. Meas. Tech.* **15**, 2325–2344 (2022).
68. D. Wunch, G. C. Toon, J. F. L. Blavier, R. A. Washenfelder, J. Notholt, B. J. Connor, D. W. Griffith, V. Sherlock, P. O. Wennberg, The total carbon column observing network. *Philos. Transact. A Math. Phys. Eng. Sci.* **369**, 2087–2112 (2011).
69. J. L. Laughner, G. C. Toon, J. Mendonca, C. Petri, S. Roche, D. Wunch, J. F. Blavier, D. W. Griffith, P. Heikkinen, R. F. Keeling, M. Kiel, The total carbon column observing network's GGG2020 data version. *Earth Syst. Sci. Data.* **16**, 2197–2260 (2024).
70. S. I. Stewart, B. Wilmer, R. B. Hammer, G. H. Aplet, T. J. Hawbaker, C. Miller, V. C. Radeloff, Wildland-urban interface maps vary with purpose and context. *J. For.* **107**, 78–83 (2009).
71. R. V. Platt, The wildland–urban interface: Evaluating the definition effect. *J. For.* **108**, 9–15 (2010).
72. J. Notholt, C. Petri, T. Warneke, M. Buschmann. TCCON data from Bremen (DE), Release GGG2020.R0 (Version R0), CaltechDATA (2022). https://doi.org/10.14291/tccon.ggg2020.bremen01.R0.
73. I. Morino, V. A. Velazco, A. Hori, O. Uchino, D. W. T. Griffith. TCCON data from Burgos, Ilocos Norte (PH), Release GGG2020.R0 (Version R0), CaltechDATA (2022). https://doi.org/10.14291/tccon.ggg2020.burgos01.R0.
74. L. T. Iraci, J. R. Podolske, C. Roehl, P. O. Wennberg, J.-F. Blavier, N. Allen, D. Wunch, G. B. Osterman. TCCON data from Edwards (US), Release GGG2020.R0 (Version R0), CaltechDATA (2022). https://doi.org/10.14291/tccon.ggg2020.edwards01.R0.
75. P. O. Wennberg, C. M. Roehl, D. Wunch, J.-F. Blavier, G. C. Toon, N. T. Allen, R. Treffers, J. Laughner. TCCON data from Caltech (US), Release GGG2020.R0 (Version R0), CaltechDATA (2022). https://doi.org/10.14291/tccon.ggg2020.pasadena01.R0.
76. D. Wunch, J. Mendonca, O. Colebatch, N. T. Allen, J.-F. Blavier, K. Kunz, S. Roche, J. Hedelius, G. Neufeld, S. Springett, D. Worthy, R. Kessler, K. Strong. TCCON data from East Trout Lake, SK (CA), Release GGG2020.R0 (Version R0), CaltechDATA (2022). https://doi.org/10.14291/tccon.ggg2020.easttroutlake01.R0.
77. K. Strong, S. Roche, J. E.Franklin, J. Mendonca, E. Lutsch, D. Weaver, P. F. Fogal, J. R. Drummond, R. Batchelor, R. Lindenmaier, E. McGee. TCCON data from Eureka (CA), Release GGG2020.R0 (Version R0), CaltechDATA (2022). https://doi.org/10.14291/tccon.ggg2020.eureka01.R0.
78. O. E. García, M. Schneider, B. Herkommer, J. Gross, F. Hase, T. Blumenstock, E. Sepúlveda. TCCON data from Izana (ES), Release GGG2020.R1 (Version R1), CaltechDATA (2022). https://doi.org/10.14291/tccon.ggg2020.izana01.R1.
79. K. Shiomi, S. Kawakami, H. Ohyama, K. Arai, H. Okumura, H. Ikegami, M. Usami. TCCON data from Saga (JP), Release GGG2020.R0 (Version R0), CaltechDATA (2022). https://doi.org/10.14291/tccon.ggg2020.saga01.R0.
80. D. F. Pollard, J. Robinson, H. Shiona. TCCON data from Lauder (NZ), Release GGG2020.R0 (Version R0), CaltechDATA (2022). https://doi.org/10.14291/tccon.ggg2020.lauder03.R0.
81. M. Buschmann, C. Petri, M. Palm, T. Warneke, J. Notholt. TCCON data from Ny-Ålesund, Svalbard (NO), Release GGG2020.R0 (Version R0), CaltechDATA (2022). https://doi.org/10.14291/tccon.ggg2020.nyalesund01.R0.
82. P. O. Wennberg, D. Wunch, C. M. Roehl, J.-F. Blavier, G. C. Toon, N. T. Allen. TCCON data from Lamont (US), Release GGG2020.R0 (Version R0), CaltechDATA (2022). https://doi.org/10.14291/tccon.ggg2020.lamont01.R0.
83. P. O. Wennberg, C. M. Roehl, D. Wunch, G. C. Toon, J.-F. Blavier, R. Washenfelder, G. Keppel-Aleks, N. T. Allen. TCCON data from Park Falls (US), Release GGG2020.R1 (Version R1), CaltechDATA (2022). https://doi.org/10.14291/tccon.ggg2020.parkfalls01.R1.
84. Y. Té, P. Jeseck, C. Janssen. TCCON data from Paris (FR), Release GGG2020.R0 (Version R0), CaltechDATA (2022). https://doi.org/10.14291/tccon.ggg2020.paris01.R0.
85. I. Morino, H. Ohyama, A. Hori, H. Ikegami. TCCON data from Rikubetsu (JP), Release GGG2020.R0 (Version R0), CaltechDATA (2022). https://doi.org/10.14291/tccon.ggg2020.rikubetsu01.R0.
86. R. Kivi, P. Heikkinen, E. Kyrö. TCCON data from Sodankylä (FI), Release GGG2020.R0 (Version R0), CaltechDATA (2022). https://doi.org/10.14291/tccon.ggg2020.sodankyla01.R0.
87. I. Morino, H. Ohyama, A. Hori, H. Ikegami. TCCON data from Tsukuba (JP), 125HR, Release GGG2020.R0 (Version R0), CaltechDATA (2022). https://doi.org/10.14291/tccon.ggg2020.tsukuba02.R0.
88. M. Zhou, P. Wang, N. Kumps, C. Hermans, W. Nan. TCCON data from Xianghe, China, Release GGG2020.R0 (Version R0), CaltechDATA (2022). https://doi.org/10.14291/tccon.ggg2020.xianghe01.R0.
89. R. Sussmann, M. Rettinger. TCCON data from Garmisch (DE), Release GGG2020.R0 (Version R0), CaltechDATA (2023). https://doi.org/10.14291/tccon.ggg2020.garmisch01.R0.
90. C. Liu, W. Wang, Y. Sun, C. Shan. TCCON data from Hefei (PRC), Release GGG2020.R1 (Version R1), CaltechDATA (2023). https://doi.org/10.14291/tccon.ggg2020.hefei01.R1.
91. F. Hase, B. Herkommer, J. Groß, T. Blumenstock, M. Ä. Kiel, S. Dohe. TCCON data from Karlsruhe (DE), Release GGG2020.R1 (Version R1), CaltechDATA (2023). https://doi.org/10.14291/tccon.ggg2020.karlsruhe01.R1.
92. T. Warneke, C. Petri, J. Notholt, M. Buschmann. TCCON data from Orléans (FR), Release GGG2020.R1 (Version R1), CaltechDATA (2024). https://doi.org/10.14291/tccon.ggg2020.orleans01.R1.

Acknowledgments: This material is based upon work supported by the NSF National Center for Atmospheric Research, which is a major facility sponsored by the National Science Foundation under Cooperative Agreement No. 1852977. We thank Schug *et al.* (*2*, *56*) for their global WUI map for 2020 and St. Denis *et al.* (*37*) for the ICS-209-PLUS data product. We thank EPA for AQS data and the MODIS MCD12Q1 team for the satellite urban land cover data. We thank A. Holder for the insightful comments on WUI fires and prescribed burning. We thank the reviewers for their helpful comments and suggestions. **Funding:** This project and W.T. (principal investigator) are supported by NOAA Atmospheric Chemistry, Carbon Cycle and Climate (AC4) Program (award number: NA22OAR4310204). D.B.P. and Y.H. acknowledge the funding support from NSF (AGS-2111428). **Author contributions:** Conceptualization: W.T., L.K.E., C.W., C.H., R.B., H.M.W., C.G., and P.F.L. Methodology: W.T., C.H., D.B.P., D.S.J., F.V., Junzhe Zhang, Y.H., Jun Zhang, and S.T. Software: W.T., Junzhe Zhang, Jun Zhang, F.V., S.T., D.B.P., Y.H., and D.S.J. Validation: W.T. and Y.H. Formal analysis: W.T., Junzhe Zhang, D.B.P., and Y.H. Investigation: W.T. and Y.H. Resources: W.T., Junzhe Zhang, Y.H., H.M.W., and P.F.L. Data curation: W.T., Junzhe Zhang, and Y.H. Visualization: W.T., Junzhe Zhang, and D.S.J. Supervision: W.T., Y.H., H.M.W., and P.F.L. Project administration: H.M.W. Funding acquisition: W.T. and Y.H. Writing—original draft: W.T., K.C.B., and C.G. Writing—review and editing: W.T., L.K.E., C.W., C.H., Y.H., D.S.J., K.C.B., B.G., R.B., F.V., C.G., H.M.W., and P.F.L. **Competing interests:** The authors declare that they have no competing interests. **Data and materials availability:** All data needed to evaluate the conclusions in the paper are present in the paper and/or the Supplementary Materials. The MUSICAv0 model code along with online tutorial is available at https://wiki.ucar.edu/display/MUSICA/MUSICA+Home and https://www2.acom.ucar.edu/event/workshop/musica-tutorial-2021. The FINNv2.5 fire emission inventory is available at https://rda.ucar.edu/datasets/ds312.9/. The Schug WUI dataset is available at https://zenodo.org/records/7941460. The WUWUI dataset is available at https://zenodo.org/records/10703310. MCD12Q1 and MOPITT data are available at https://search.earthdata.nasa.gov/. TCCON data are available at https://tccondata.org/. EPA AQS data are available at https://www.epa.gov/aqs.

Submitted 22 June 2024
Accepted 7 February 2025
Published 14 March 2025
10.1126/sciadv.adr2616